Interface roughness effect on slow cyclic annular shear of granular materials

Georg Koval, François Chevoir, Jean-Noël Roux, Jean Sulem, Alain Corfdir

Noname manuscript No.
(will be inserted by the editor)

Interface roughness effect on slow cyclic annular shear of granular materials

Georg Koval, François Chevoir, Jean-Noël Roux, Jean Sulem and Alain Corfdir

Received: date / Accepted: date

Abstract We experimentally investigate the mechanical behaviour in cyclic shear of a granular material near a solid wall in a pressure controlled annular shear cell. The use of a model system (glass beads and sawtooth shaped solid surface) enables the study of the influence of the wall roughness. After an initial shakedown procedure ensuring reproducible results in subsequent tests, wall shear stress S, volumetric variation ΔV, and the displacement field of the sample bottom surface, are recorded as functions of wall displacement. A dimensionless roughness parameter R_n is shown to control the interface response. The local grain-level or mesoscale behaviour is directly correlated to the global one on the scale of the whole sample.

1 Introduction

The interaction between granular and continuum materials is often encountered in engineering problems. In geotechnical engineering the transfer of stresses between granular soil and structures is determined by the interface behaviour in systems like reinforced earth, foundations, retaining wall, etc. In such applications the mobilization of the friction and the capacity of stress transmission are important design parameters.

Considering its practical significance, the interface behaviour has been addressed in many experimental studies [1–6]. From a macroscopic viewpoint one is interested in describing the mobilization of shear stress, depending on the density or other state variables characterizing the confined granular material. Cyclic shear tests [2,7] also revealed the influence of the amplitude of tangential displacement and of the number of loading cycles on the stress response. Further studies [3–6] evidenced and quantified a discontinuity between the solid surface and the granular material displacements suggesting local singular behaviour at the interface. Shear bands were visualized by measurements of particle motion near the interface [8]. More recently, a correlation image velocimetry (CIV) algorithm [9–11] was applied to identify the deformation of a granular sample outside the shear band in an annular shear apparatus in ref. [12]. In Couette cells [12–16], this band is localized near the inner cylinder wall because of the shear stress decay in the radial direction [14].

In the present study we use the same $3D$ cylinder apparatus as in Ref. [12], i.e., a Couette cell surrounded by a flexible membrane through which a controlled radial pressure is imposed. We focus on the interfacial zone, in the immediate vicinity of the solid shearing surface. Our main objective is to identify the relations between the characteristics of the shear band, the macroscopic and the mesoscopic shear behaviours and the influence of the surface roughness.

A general description of the cylinder cell, of the sample material and of the experiments are presented in Sec. 2. The experimental procedure is presented in Sec. 3. Sec. 4 then deals with the macroscopic behaviour

G. Koval
Université Paris-Est, Laboratoire Navier (ENPC/LCPC/CNRS), École des Ponts Paristech, 6 & 8 av Blaise Pascal, 77455 Marne-la-Vallée, France

Present address:
G. Koval
Institut National des Sciences Appliquées, 24 bd de la Victoire, 67084 Strasbourg, France
E-mail: georg.koval@insa-strasbourg.fr

A. Corfdir
Université Paris-Est, Laboratoire Navier (ENPC/LCPC/CNRS), École des Ponts Paristech, 6 & 8 av Blaise Pascal, 77455 Marne-la-Vallée, France
E-mail: corfdir@cermes.enpc.fr

observed, while the mesoscopic (local scale) results are presented in Sec. 5. Finally, we discuss the main results in Sec. 6 and state our conclusions in Sec. 7.

2 Material characteristics and description of the geometry

2.1 Device principle

The cylindrical simple shear device (ACSA, in French) was designed and constructed (in the CERMES laboratory) in 1993. Detailed information, including related theoretical considerations, material description, experimental results and numerical simulations can be found in two doctoral dissertations [17,18] and a series of related publications [19–22].

The device operating principle is based on shearing a confined annular sample by the rotation of a rigid internal cylinder, as shown in Fig. 1. The sample has internal radius $R_i = 100$ mm (defined naturally by the internal cylinder radius), outer radius $R_o = 200$ mm and height H equal to $R_o - R_i = 100$ mm.

A controlled angular velocity of the cylinder imposes tangential velocity $V_\theta = 2$ mm/min to the sample internal surface. On the outer surface, a radial confining pressure, P_r, is applied (at R_o), and a vertical pressure, P_z, is applied onto the top.

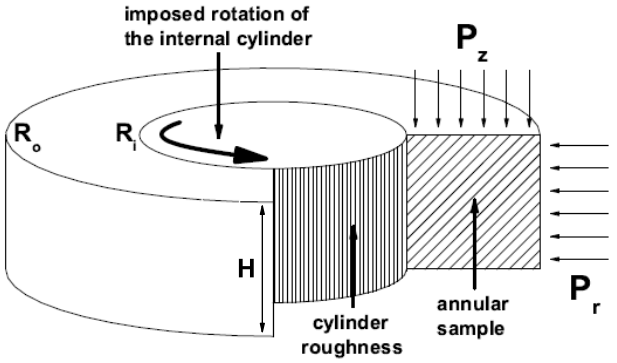

Fig. 1 *Scheme of the annular cell.*

Complementary information concerning the annular shear device is provided in Appendix A.

2.2 Granular material

Dry glass beads assemblies are chosen as model, well controlled granular materials. Different diameters d are used, with nearly monodisperse population of beads: 0.25, 0.5, 1.8 and 8 mm (see table 1).

As confining pressures are maintained below 150 kPa our experiments do not show any sign of particle attrition or damage.

2.3 Internal cylinder

The roughness of the internal cylinder surface is composed of a set of vertical triangular striations, with wavelength L_1 and groove depth L_2, as defined in Fig. 2. Two different cylinders are used: cylinder 1, with $L_1 = 1.7$ mm and $L_2 = 1$ mm, and cylinder 2, with $L_1 = 0.44$ mm and $L_2 = 0.1$ mm.

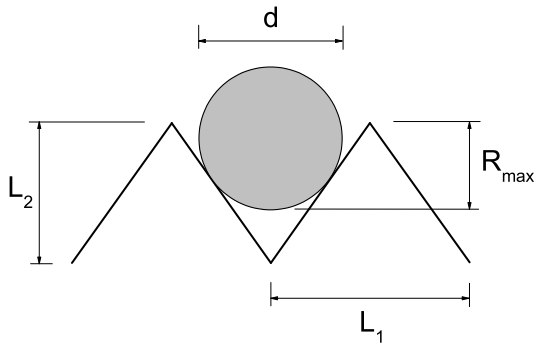

Fig. 2 *Triangular striation parameters and maximum particle penetration R_{max}.*

2.4 Normalized roughness

We use the same normalized roughness parameter as introduced in Ref. [23]. We denote as $R_{\max}$ the elevation difference between the deepest and the highest possible contact points on the rough surface, as shown in Fig. 2. The normalized roughness is then defined as $R_n = R_{\max}/d$.

In Fig. 3, we distinguish two different types of contact, depending on the values of d, L_1 and L_2. Denoting a threshold particle diameter as $d_{\lim} = \frac{L_1}{L_2}\sqrt{\left(\frac{L_1}{2}\right)^2 + (L_2)^2}$, the particles mostly enter in contact with facets of the rough wall if $d \leq d_{\lim}$, while for $d \geq d_{\lim}$ they only touch the teeth tips. The normalized roughness R_n depends on d, L_1, L_2 as

$$\begin{aligned} R_n &= \frac{1}{2} + \frac{L_2}{d} - \sqrt{\frac{1}{4} + \left(\frac{L_2}{L_1}\right)^2} \text{ if } d \leq d_{\lim} \\ R_n &= \frac{1}{2} - \frac{1}{d}\sqrt{\left(\frac{d}{2}\right)^2 - \left(\frac{L_1}{2}\right)^2} \text{ if } d > d_{\lim} \end{aligned} \quad (1)$$

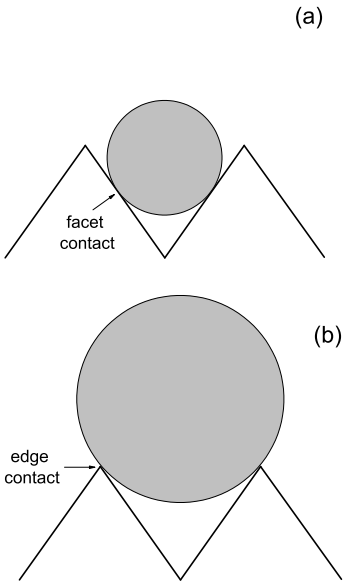

Fig. 3 *Particle-wall contact for (a) $d \leq d_{lim}$ and (b) $d > d_{lim}$*

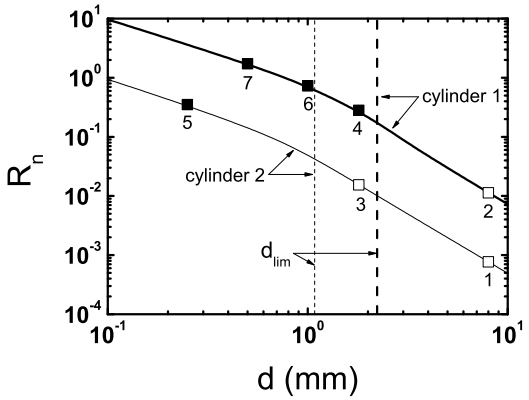

Fig. 4 *Normalized roughness R_n as a function of particle diameter d for both cylinders (Eq. 1). The vertical lines indicate the limit diameter d_{lim} for each cylinder. The filled symbols represent the samples with $d \leq d_{lim}$, while the hollow ones, the samples with $d > d_{lim}$.*

2.5 List of samples

The list of samples with geometric data (including roughness parameter R_n) is drawn up in Table 1.

Experiment	d (mm)	cylinder	R_n	R_i/d
1	8.0	2	$7.72.10^{-4}$	12.5
2	8.0	1	$1.14.10^{-2}$	12.5
3	1.8	2	$1.55.10^{-2}$	55.5
4	1.8	1	$2.82.10^{-1}$	55.5
5	0.25	2	$3.52.10^{-1}$	400.0
6	1.0	1	$7.27.10^{-1}$	100.0
7	0.5	1	1.73	200.0

Table 1 *List of experiments with corresponding roughness level R_n and geometric parameter R_i/d.*

In Fig. 4, roughness parameters R_n are shown for all experiments, depending on the bead diameter for both cylinders.

3 Experimental procedure and measurements

3.1 Cyclic shear procedure

The slowly rotation of the central cylinder transmits the shear stress to the material sample, which is maintained under prescribed radial and vertical pressures. The different sensors composing our experimental setup provide macroscopic (sample scale) measurements of the shear stress at the inner wall S and of the sample volumetric variation ΔV. These data are recorded along with wall tangential displacement D, providing detailed information on friction mobilization in an entire cycle.

As discussed in Appendix B, a cyclic procedure is suitable to prepare samples that are independent of the deposition and preconsolidation processes. After a sufficient number of shear reversals, the stress and the volumetric behaviour of the material become identical from one cycle to the next. The cycles then superimpose and exhibit the shape schematized in Fig. 5. Displacement amplitude a (see discussion in Sec. B.2) is set to 5 cm.

3.2 Normalized volumetric variation ΔV_n

Considering previous results [12,24,25], and anticipating on Section 5, we assume that, at least once the cyclic behaviour gets stabilized at the end of the preparation procedure, shear strain and volume changes are localized near the interface. Consequently, volume changes ΔV should not be compared to the total sample volume, but rather to the volume of the interface region, i.e.,

$$V_b = A_p \; L_b, \tag{2}$$

where L_b is the shear band thickness and $A_p = 2\pi R_i H$ is the wall surface area. Thus the sample volumetric variation ΔV reads:

$$\Delta V = \Delta V_b = A_p \; \Delta L_b, \tag{3}$$

and the variation of shear band thickness, relative to the particle size, is given by the *normalized volumetric variation* ΔV_n, defined as:

$$\Delta V_n = \frac{\Delta V}{A_p \; d} = \frac{\Delta L_b}{d}. \tag{4}$$

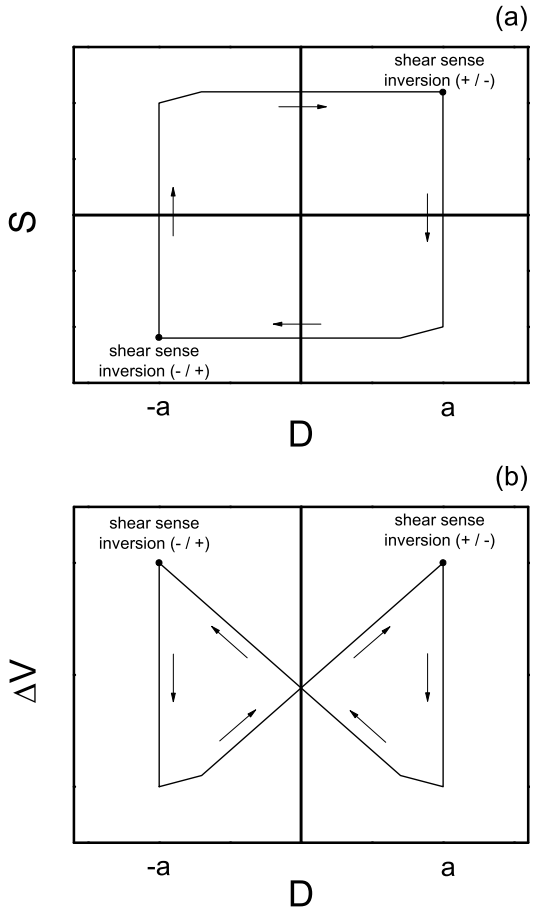

Fig. 5 *Schematic behaviour (a) of shear stress at the wall S and (b) of volumetric variation ΔV in stabilized cycle.*

3.3 Confining pressures

Each sample is subjected to 3 different configurations of the confining pressure. The average vertical pressure is maintained constant $P_z = 100$ kPa in all cases, while the radial component P_r takes the values: 67 (C_1), 100 (C_2) and 150 kPa (C_3), as summarized in Table 2.

Load	P_r (kPa)	P_z (kPa)
C_1	67	100
C_2	100	100
C_3	150	100

Table 2 *Vertical and radial pressures for the three applied loads.*

The effect of different load configurations, as discussed in Appendix C, is approximately accounted for on defining an *effective pressure* as

$$P = (P_r + P_z)/2. \tag{5}$$

The ratio of the shear stress to the effective pressure then defines the *apparent coefficient of friction*

$$\mu^*_{\rm app} = S/P. \tag{6}$$

Those definitions are discussed in Sec. 4.1.

3.4 Velocimetry

During each shear experiment, series of photographs are taken through the window at the base plate (Fig. 6), in order to study the local effects of shearing. Images are recorded over 2.5 cycles. We thus have 5 sequences of pictures, covering a tangential displacement of 10 cm (-5 cm $\leq D \leq 5$ cm) in each half cycle. This procedure is repeated for each load (C_1, C_2 and C_3). Correlation image velocimetry (CIV) [9–12] is implemented to identify the velocity field at the bottom surface of the sample. Considering a polar coordinate system (r, θ) with its origin at the center of the internal cylinder, we analyzed the tangential component of the velocity v_θ in experiments 1, 2, 4, 6 and 7.

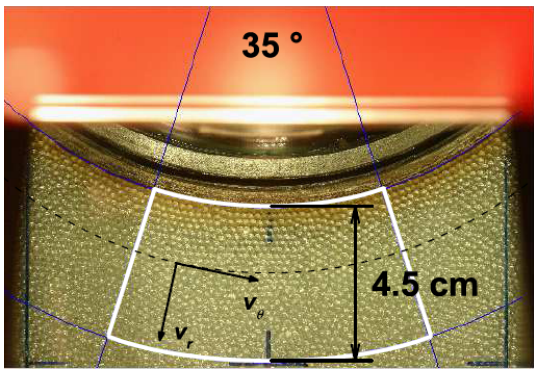

Fig. 6 *Base plate opening for sample visualization. The region within which velocity (with its polar coordinates as sketched) is measured is framed in white.*

On analyzing successive pairs of images, we determine the mean displacement vector in regions of 64×64 pixels ($\approx 2.8 \times 2.8$ mm), spaced horizontally and vertically by 32 pixels (≈ 1.4 mm).

The resolution of the photographs (3072×2048 pixels) allows us to study the displacements at the particle scale. The CIV method requires small displacements between the images, not exceeding 1/4 of the region size [26]. With a time interval of 6 s between two successive images and wall tangential velocity $V_\theta = 2$ mm/min, the maximum displacement is well below this upper limit.

Tangential displacements are extracted and averaged within an angular sector of 35° at constant radial

coordinate r, whence a radial profile of the tangential displacement, or, equivalently, a radial profile of tangential velocity, $v_\theta(r)$, averaged over a small time interval. Those profiles characterize a mesoscopic scale, over which local values of macroscopic field variables can tentatively be identified.

Magnetic resonance imaging in an annular shear device [27] showed that profiles $v_\theta(r)$ were but negligibly affected by the vicinity of the top and bottom smooth plates. The same conclusion was reached from confocal images of a similar apparatus [7]. **Rougher plates, however, may disturb the velocity profiles [27]. The possible effects of the glass plates are discussed in Sec. 6.2.2.**

4 Macroscopic results

Our results on the macroscopic response of the interface under cyclic shear, as expressed by shear stress S and volume variation ΔV_n, are presented below. We first investigate the effects of interface roughness and confining load in Sec. 4.1. In Sec. 4.2, we give a qualitative description of the observed cyclic behaviour, where two classes of response are distinguished. A discussion about the interface coefficient of friction is presented in Sec. 4.3, while some aspects of the friction mobilization are analyzed in Sec. 4.4. Finally the influence of the normalized roughness R_n over the volumetric behaviour is presented in Sec. 4.5.

4.1 Shear stress at the wall S

As in recent experiments, with ACSA [28] or other devices [1,29–31], we observe wall shear stress S to increase with the roughness level. In Fig. 7a, the maximum value wall shear stress in the cycle, denoted as S_4, corresponding to the plateau ending in the inversion point in graph 5a, is shown as a growing function of normalized roughness R_n. **Figs. 7a and 7b reveal the influence of the confining pressure: effective pressure P (Eq. 5) appears to successfully combine the influence of P_r and P_z on normal stresses at the wall, so that, as shown by the superposition of curves in plot 7b, an apparent coefficient of friction $\mu^*_{\mathbf{app}}$ (Eq. 6) can in fact be identified (see further discussion in Sec. 4.3).**

4.2 Rough and smooth behaviour in shear cycle

On comparing the observed variations of wall shear stress and volume changes ΔV_n versus displacement D in stabilized cycles, as previously schematized in Fig. 5, a qualitative classification of the macroscopic interface layer response into rough and smooth categories emerges, as illustrated by Fig. 8.

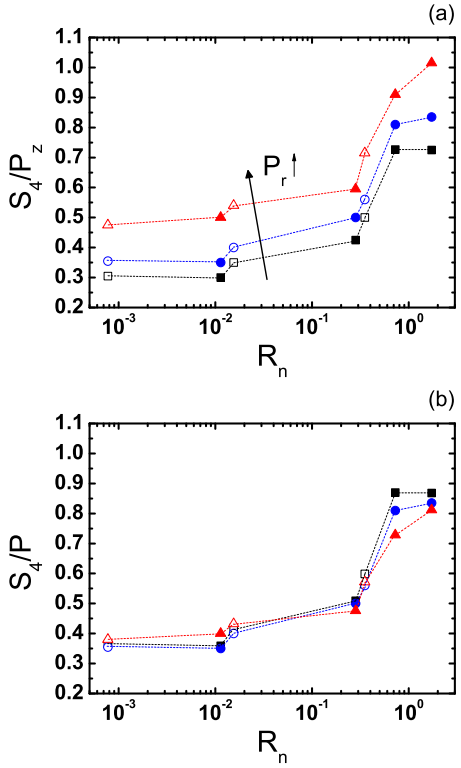

Fig. 7 *Influence of the normalized roughness R_n over the shear stress normalized (a) by the vertical confining pressure value S/P_z, and (b) by the effective confining pressure S/P for different loads: (■,□) C_1, (●,○) C_2 and (▲,△) C_3. The filled symbols correspond to the cylinder* 1*, while the hollow ones, to the cylinder* 2*.*

We define reference points, labeled 1 to 4 (see Fig. 8), in each half-cycle (corresponding to monotonic wall displacement). The material first exhibits a contracting behaviour after point 1, while S varies rapidly with D. At *point 2*, the volume ceases to decrease, reaching a minimum plateau, while $|S|$ keeps increasing. Then, starting at *point 3*, dilation is observed, while S approaches an asymptotic value. For the larger values of roughness parameter R_n, this evolution occurs in two stages, whence the definition of *points 3a and 3b* in Fig. 8B, and we use this qualitative feature to distinguish rough interfaces from smooth ones. Between points 2 and 3a, both S and ΔV_n vary rapidly, considerably faster than in the typical smooth cases (compare plots labeled a and c on parts A and B of Fig. 8). The observed dilatancy beyond point 3b suddenly becomes much smaller (similar to the smooth case value). A similar change of slope is apparent at point 3b on

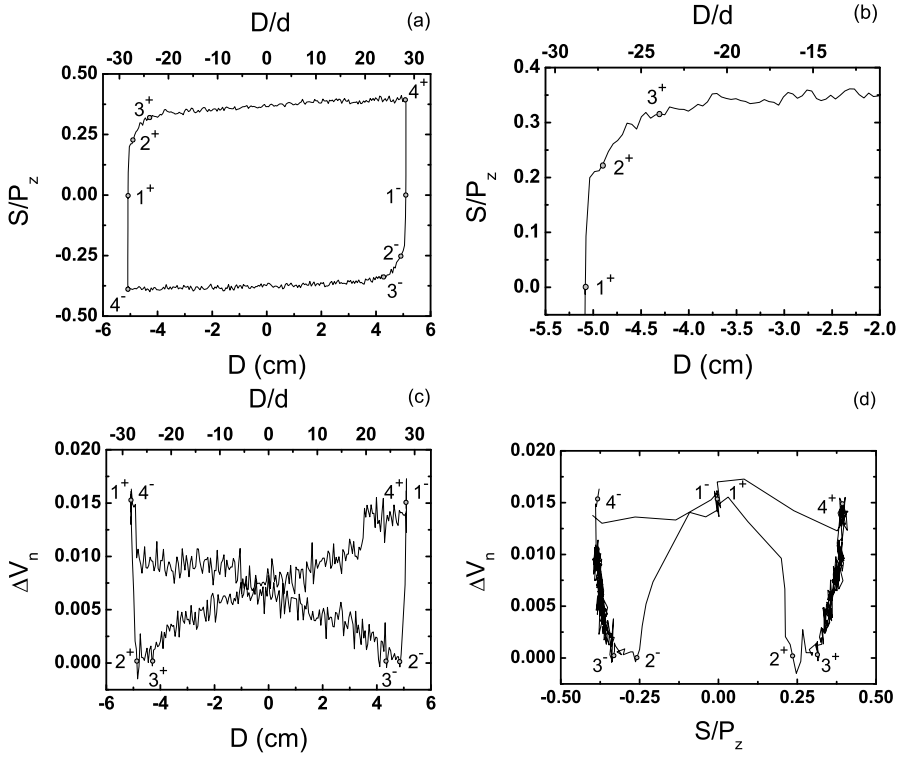

(A) Smooth interface case (experiment 3).

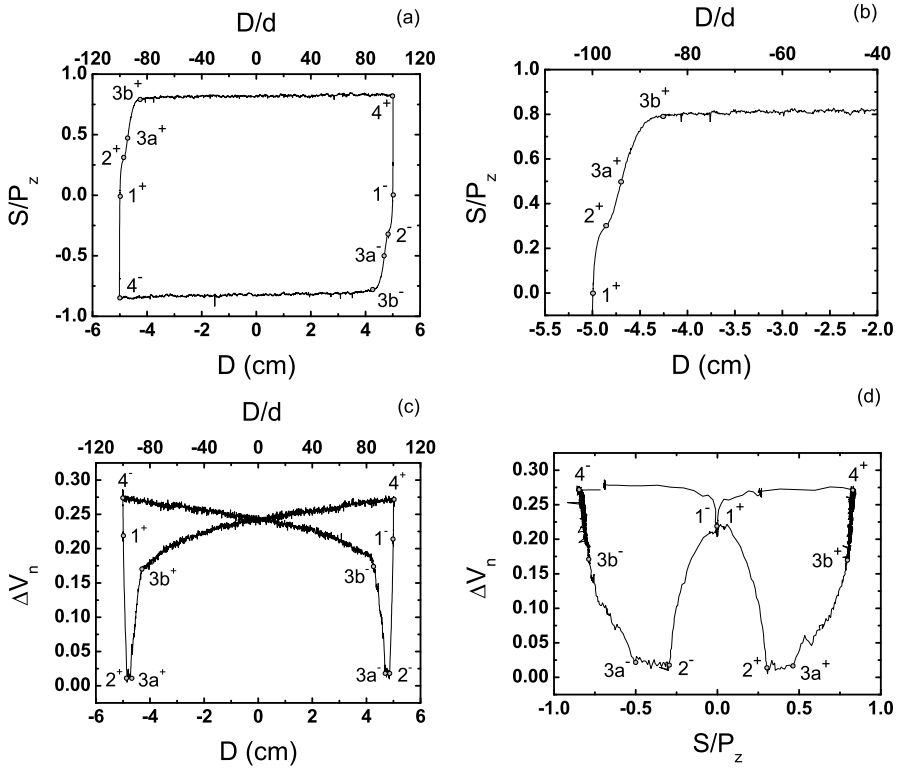

(B) Rough interface case (experiment 7).

Fig. 8 *Interface behaviour in shear cycle (A, top four plots) in smooth and (B, bottom plots) rough cases. (a) S/P_z (with initial fast variation in (b)) and (c) normalized volume variation ΔV_n vs. wall displacement D. (d) ΔV_n vs. S/P_z. Symbols + and − following reference point numbers on graphs indicate sign of wall velocity.*

the S versus D plot. After point 3 (smooth case), or point 3b (rough case), both S and ΔV_n approach a plateau. *Point 4* (whence notation S_4 used in Sec. 4.1) is the shear strain reversal point, where the inner cylinder starts rotating in the opposite direction. In the final part of the cycle, from point 4 back to point 1, S displays a very fast (unloading) variation with D.

Table 3 classifies all seven interface tests into smooth and rough interface categories.

Experiment	R_n	*Behaviour*
1	0.000772	smooth
2	0.0114	smooth
3	0.0155	smooth
4	0.282	smooth
5	0.352	smooth
6	0.727	rough
7	1.73	rough

Table 3 *Sample interface classification according to macroscopic behaviour during cycle shear.*

4.3 Apparent coefficient of friction $\mu^*_{\rm app}$

The values of the apparent coefficient of friction $\mu^*_{\rm app}$ for characteristic points 2, 3 or 3a and 4 are given in Fig. 9 for different values of normalized roughness R_n. Coefficient $\mu^*_{\rm app}$ increases with roughness level R_n, the fastest in the range of $R_n \sim 0.1$, approaching an upper limit as $R_n \geq 0.7$. A similar result was observed in [32], also with glass beads, indicating a limited influence of the normalized roughness over the stresses for $R_n \geq 0.5$. It was shown in that study that the maximum interface coefficient of friction is limited by the internal coefficient of friction of the material ($\mu^*_0 \leq 0.58$ for glass beads [32]). Normal and shear stresses were both measured, providing in fact a real (in contrast to apparent) effective coefficient of friction at the interface. In our case, the volume variation during the cyclic shear, especially for rough interfaces (see Sec. 4.2 just above), might also cause an increase of the normal stress at the interface, whence the observation of $\mu^*_{\rm app} > \mu^*_0$ for rough interfaces in our experiments. In the opposite limit of very smooth interfaces, as $R_n \lesssim 0.01$ (in agreement, again, with the experiments of [32]), $\mu^*_{\rm app}$ approaches an R_n-independent lower asymptotic value (clearly visible in Fig. 7b for $\mu^*_{\rm app} \simeq S_4/P$ associated to characteristic point 4).

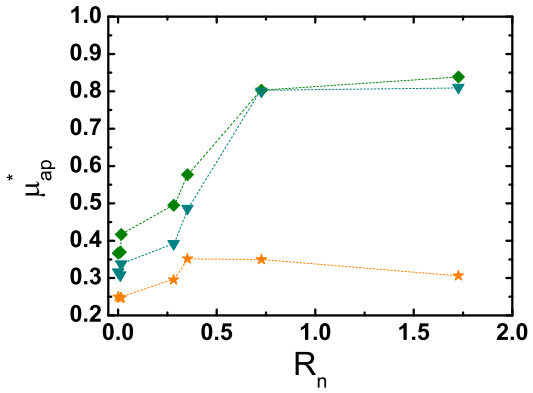

Fig. 9 *Apparent effective coefficient of friction μ^*_{app} for different reference points: (⋆) 2, (▼) 3 or 3a and (◆) 4.*

4.4 Friction mobilization distance

We call friction mobilization distance the necessary displacement (from the beginning of the cycle, point 1, where $S = 0$) to reach a certain shear stress level at the wall. Thus, to the shear stresses S_2 and S_3 we respectively associate mobilization distances l_{12} and l_{13}.

Fig. 10 shows mobilization distances normalized by the particle diameter, l_{12}/d and l_{13}/d, as functions of R_n for the 3 different loads, evidencing a growing trend already reported in [28]. **Both distances keep increasing (with no apparent upper limit, unlike shear stress S) for the largest investigated roughness levels. Inferior limits observed for $R_n \to 0$ indicate the effect of the friction of a totally smooth cylinder. The mobilization of the friction would induce some particle rearrangement: maximum compaction in a shear distance of $l_{12}/d \approx 1.50$; beginning of the dilation in $l_{13}/d \approx 4.00$. At the end of a cycle, the shear stress transmitted to the particles would correspond to $S_4/P \approx 0.35$ (see Fig. 7b).**

4.5 Influence of R_n on ΔV_n

As a global characteristic of volumetric behaviour, we take the maximum amplitude of the variation of ΔV_n in a cycle, equal to ΔV_n^{2-4}, its variation between points 2 and 4 (see Figs. 8Ac or 8Ad and 8Bc or 8Bd). Fig. 11 shows an approximately linear dependence of this variable on normalized roughness R_n. The low values of ΔV_n^{2-4}, observed for smooth interfaces (Fig. 11), are correlated to the corresponding low values of the shear stress (Fig. 7c) and of the friction mobilization length (Fig. 10).

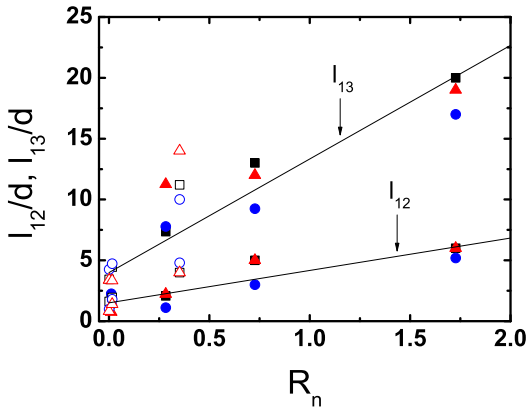

Fig. 10 *Normalized friction mobilization distances l_{12}/d and l_{13}/d for different loads: (■,□) C_1, (●,○) C_2 and (▲,△) C_3, as functions of normalized roughness R_n, in tests with cylinders 1 (filled symbols) and cylinder 2 (hollow symbols). Fit functions: $l_{12}/d = 2.67R_n + 1.50$ and $l_{13}/d = 9.33R_n + 4.00$ are plotted with solid lines.*

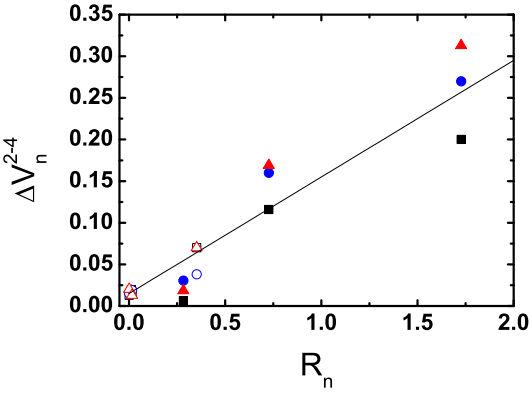

Fig. 11 *Normalized volumetric variation ΔV_n^{2-4} as a function of the normalized roughness R_n for different loads: (■,□) C_1, (●,○) C_2 and (▲,△) C_3. The filled symbols correspond to the experiments with the cylinder 1, while the hollow ones, to the experiments with the cylinder 2. The solid line indicates the function $\Delta V_n^{2-4} = 0.14R_n + 0.015$.*

5 Mesoscopic results - Velocity field

We now present our mesoscopic results (i.e. quantities measured at the scale of a few particles), based on the radial profiles of the particle tangential velocity (see 3.4). We derive from them the sliding of particles at the interface and the shear band thickness.

5.1 Thickness of the shear band λ^+

The thickness of the shear band is derived from the characteristics of the velocity profile. We observe a discontinuity between the velocities of the wall V_θ and of the particles surrounding the wall $V_\theta^+ = v_\theta(R_i)$ (where R_i is the radial coordinate of the wall). Then we define the thickness of the shear band λ^+ as the length where we get a decrease of 90% of the particle velocity V_θ^+ (Fig. 12):

$$v_\theta(\lambda^+ + R_i)/V_\theta^+ = 0.1, \tag{7}$$

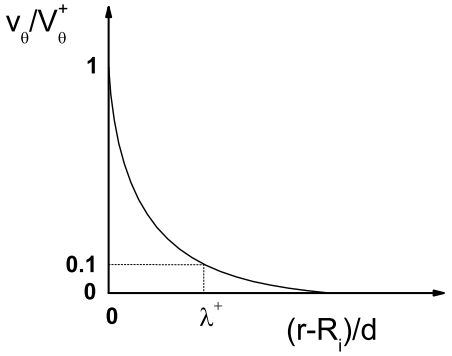

Fig. 12 *Definition of shear band thickness λ^+.*

5.2 Evolution of velocity profile $v_\theta(r)$ in cyclic shear

During the cycles, we observed the evolution of the shear stress at the wall S and of the normalized volumetric variation ΔV_n as a function of the wall displacement D as previously discussed in Sec. 4.

In order to evaluate the evolution of the radial profile of the tangential velocity $v_\theta(r)$, we divide a half cycle ($-5\ cm \leq D \leq 5\ cm$) into 11 intervals. Within each interval, we determine the time-averaged velocity profile v_θ. The 10 first intervals correspond to segment -5 cm $\leq D \leq -3$ cm ($10 \times 0.2\ cm$) of the half cycle. The last one (-3 cm $\leq D \leq 5$ cm) provides a stationary profile of reference.

Fig. 13b shows profiles $v_\theta(r)/V_\theta$ within those intervals, visualized with the dotted lines on Figs. 13a and 13c. Similar to the evolution of S, a stationary velocity profile is approached at large D.

As shown in Fig. 13b, the particle slip at the interface is constant within the stabilized cycle, although an evolution of this parameter before the stabilization was reported in other studies [3,4].

Fig. 13d, the level of shear localization is characterized by λ^+, the shear band thickness as defined in Sec. 5.1. λ^+ decreases from the beginning of the cycle, approximately as:

$$\lambda^+ = \lambda_s^+ \left(1 + m \exp\left[-n(D - D_0)/d\right]\right), \tag{8}$$

where λ_s^+ is the stationary value of λ^+ and D_0 is the initial position of the (half) cycle ($D_0 = \pm a$, see Sec. 3.1). The parameter n is the characteristic displacement of the wall regarding the evolution of the strain localization. The value of m indicates the difference between transient and steady profiles. Shear band thickness λ^+ tends to its steady state value λ_s^+ side by side with the behaviour change of the shear stress S and of the volumetric variation ΔV_n to a slow evolution (point 3b). A similar, but only qualitative observation have been made by [7]. The influence of the material density on the localization phenomenon was evidenced by [33].

Chambon et al. [12] measured correlated displacements far from the wall before localization, in the beginning of the shear test, showing that a thicker region is then mobilized. They evidenced a transition in the bulk outside the shear band for $(D - D_0)/d \simeq 25$. This value corresponds to the displacement for which λ^+ closely approaches its steady-state plateau.

5.3 Stationary velocity profiles $v_\theta(r)$

5.3.1 General behaviour

We now compare the different profiles of tangential velocity v_θ measured in experiments 1, 2, 4, 6 and 7 (for all 3 loads C_1, C_2 and C_3). The profiles are averaged between points 3 (or 3b) and 4, and we regard them as characteristic of a steady state.

Profile $v_\theta(r)$, decays approximately as an exponential away from the inner cylinder [12,13,15,34]. Some profiles (experiments 1 and 2) exhibit considerable oscillations with a wavelength equal to the particle diameter. This is mainly due to particle rotation and exists in all systems. The resolution of the CIV method is of the order of several diameters for smaller grains, explaining the apparent absence of oscillations in these cases. Oscillations on the grain scale were also reported in other studies [35,36]. As shown in Fig. 14, the profiles are almost identical for all three types of load (C_1, C_2 and C_3).

The effects of the normalized roughness R_n and of system size R_i/d are dealt with in the following paragraphs.

5.3.2 Sliding

Profiles $v_\theta/V_\theta(r)$ are plotted in Fig. 14. Sliding at the wall is characterized by a tangential velocity discontinuity, and it increases when the interface roughness decreases as shown in Fig. 15. Ratio V_θ^+/V_θ is approximately equal to 0.75 for $R_n \geq 0.7$, and varies roughly

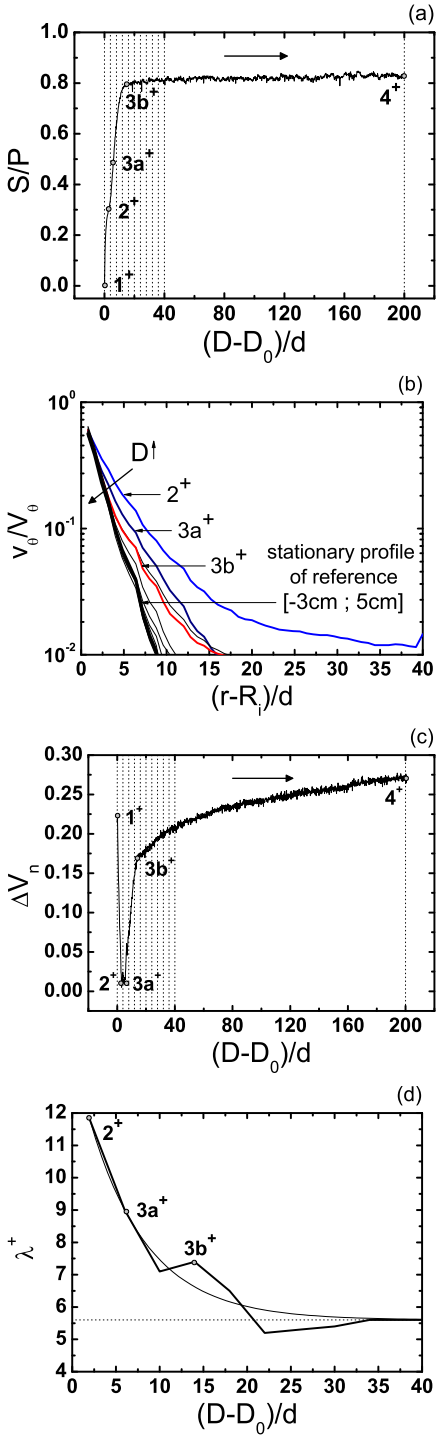

Fig. 13 *For experiment 7, (a) shear stress at the wall S and (c) normalized volumetric variation ΔV_n as functions of displacement D. The arrows indicate the sense of increasing D. The vertical dotted lines mark intervals within the half cycle ($10 \times 0.2\ cm + 1 \times 8\ cm$) over which velocities are averaged, resulting in the profiles plotted in (b). (d) Shear band thickness λ^+ versus displacement. The dotted line gives the stationary value. The solid line is a fit (Eq. (8)) with $\lambda_s^+ = 5.6$, $m = 1.5$ and $n = 0.17$.*

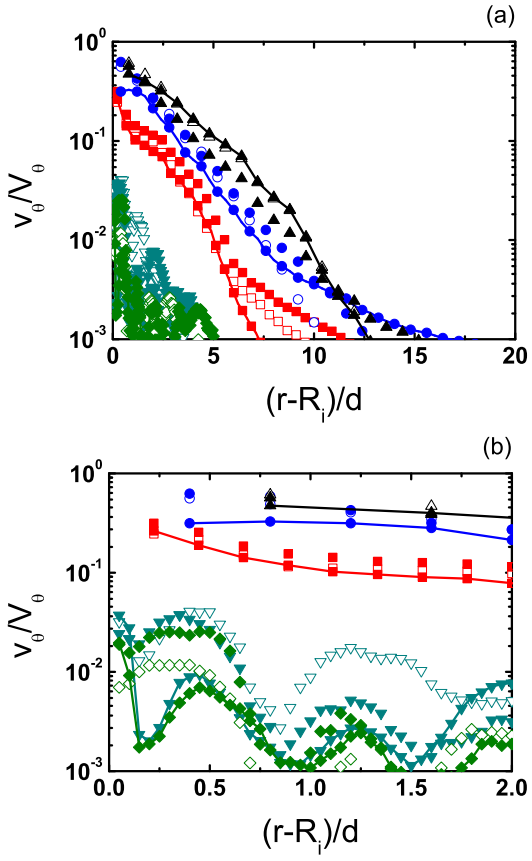

Fig. 14 *(a) Velocity $v_\theta/V_\theta(r)$ versus dimensionless distance from the wall $(r-R_i)/d$ ((b) detail of the zone close to the wall). Different experiments: (◇, ◆, −◆−) experiment 1, (▽, ▼, −▼−) experiment 2, (□, ■, −■−) experiment 4, (○, ●, − ● −) experiment 6, (△, ▲, −▲−) experiment 7. The hollow symbols correspond to load C_1, the filled ones to load C_2 and the connected ones to C_3.*

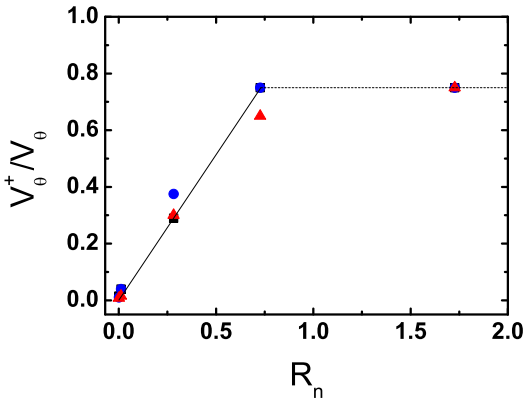

Fig. 15 *Ratio V_θ^+/V_θ (sliding parameter) as a function of normalized roughness R_n for different loads: (■) C_1, (●) C_2, (▲) C_3. The solid line is the linear function $V_\theta^+/V_\theta = 1.05R_n$.*

linearly with R_n for lower roughness levels. The numerical simulations of [37] indicated more complex relations between V_θ^+/V_θ and R_n (depending on the system characteristics, V_θ^+/V_θ tends to a constant value when $R_n \to 0$).

6 Discussion of the results

6.1 Smooth and rough behaviour

We have presented different aspects of shear behaviour. We now discuss the transition from smooth to rough behaviour as R_n increases. The analysis of various parameters shows two distinct responses considering the interface roughness: smooth, for lower values of R_n, and rough, for higher ones. The transition seems to be located between 0.35 (experiment 5) and 0.73 (experiment 6).

Cyclic response. The shear stress and the volumetric responses of the sample present a similar cyclic shape, however for $R_n \geq 0.73$ we identified an additional dilation phase (segment $3a-3b$ in Fig. 8Bc). The stronger dilation observed in the rougher cases is followed by a stronger compaction (segment $4-1$ in Fig. 8Bc).

Shear stress values. Values of the shear stress (S_3 and S_4) clearly approach an upper limit for $R_n \geq 0.73$. For very low values of roughness ($R_n \leq 0.01$), the observation of a lower limit value suggests that one may distinguish smooth, "intermediate" and rough behaviour.

Friction mobilization distance and volumetric variation. Both parameters seem to gradually increase with R_n.

Sliding. As already seen for the macroscopic results, the velocity profile is also affected by the interface roughness. The main effect can be analyzed through the discontinuity of the velocity at the wall, characterized by ratio V_θ^+/V_θ. This ratio decreases as R_n increases, with a rough and a smooth limit that appear to be correlated to the shear stress behaviour.

6.2 Geometric effects

Beyond the effect of the roughness of the wall, its curvature may affect the behaviour of the material near the interface [14]. As shown by [37], parameter R_i/d (ratio of inner radius to particle size) influences the local material deformation close to the wall and the shear band thickness.

6.2.1 Velocity profile $v_\theta/V_\theta(r)$

The analysis of the velocity profiles normalized by the maximum tangential velocity of the particles, V_θ^+, instead of the wall velocity V_θ, allows us to compare the shape of the velocity profiles in different experiments, while minimizing the effects of normalized roughness R_n (such as, in particular, sliding). This comparison is presented in Fig. 16, in which, for clarity, results pertaining to C_1, C_2 and C_3 are averaged over (given the negligible effect of the loading over the velocity profiles). The profiles of in Fig. 16a were fitted to an exponential form, $v_\theta/V_\theta^+ = \exp[-t(r - R_i)/d]$ to the profiles shown in Fig. 16a (except for the results of experiment 1, which still exhibit fluctuations).

The observed shear band gets thicker (in particle diameters) for increasing R_i/d (see Fig. 16a). However, in absolute scale, the shear band is in fact thinner for increasing R_i/d (as we can see in Fig. 14b, with the cylinder radius as characteristic length unit for all experiments). A similar effect of R_i/d over the strain localization length was also reported in the numerical study of [36].

6.2.2 Shear band thickness

The shear stress is larger for smaller values of R_i/d, which explains the stronger strain localization near the shearing wall [36]. Therefore shear band thickness λ_s^+ tends to increase for larger R_i/d as indicated by our results in Fig. 17. In a plane shear experiment (i.e., in the limit of $R_i/d \to \infty$), the shear band invades the whole geometry, while in the opposite limit of small R_i/d, λ_s^+ tends to zero. The values of λ_s^+ shown in Fig. 17 are based on the exponential approximations (Fig. 16a) to avoid the effect of the remaining oscillations, in spite of the averaging. We observe in this case a dependence of λ_s^+ as a power-law function of R_i/d, consistent with the results of [36] in the quasi-static regime.

The proximity of the base plate can disturb the velocity profiles, causing an apparent diminution of shear band thickness due to the surface friction. The results of [27] suggest that the effect of the bottom plate may depend on the relation between the cylinder and the surface roughness. The shear band obtained with a rough cylinder and a smooth plate were only affected by a reduction of about 5% close to the plate. However, a rough plate caused a reduction of about 53% in similar conditions. Considering crudely these both values as minimum and maximum relative reductions of the shear band thickness, we plot an estimation (dashed line) of λ_s^+ far from the bottom plate in Fig. 17. Those values represent an overestimation of the plate disturb of our measures, since the glass plate is considerably smoother than the striated metallic cylinder 2 used in our experiments.

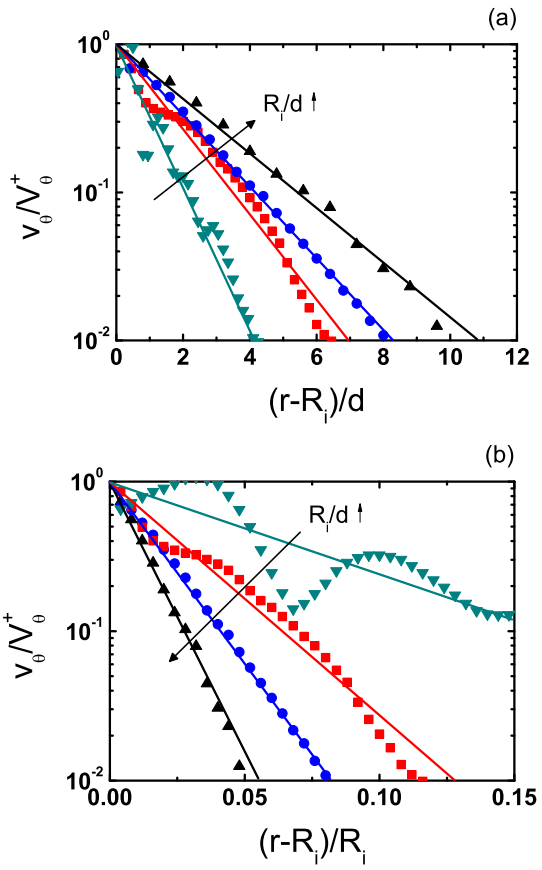

Fig. 16 *$v_\theta/V_\theta^+(r)$, versus the distance from the wall, normalized (a) by the particle diameter, $(r - R_i)/d$, and (b) by the radius of the cylinder, $(r - R_i)/R_i$. Different experiments: (▼) experiment 2 ($R_i/d = 12.5$), (■) experiment 4 ($R_i/d = 55.5$), (●) experiment 6 ($R_i/d = 100$), (▲) experiment 7 ($R_i/d = 200$). Results average over C_1, C_2 and C_3 data. Solid lines are exponential fits.*

6.3 Relation between volumetric variation and particle sliding

Our definition of normalized volumetric variation ΔV_n (Sec. 3.2) assumes changes in density to be concentrated close to the shearing wall, so that ΔV_n is directly related to shear band thickness variation: $\Delta V_n = \Delta\lambda^+$. In a half cycle of length $2a$ (Sec. 3.1), the shear band distortion (or shear strain), γ should be proportional to the ratio of tangential displacement aV_θ^+/V_θ to steady-state shear band (absolute) thickness $\lambda_s^+ d$:

$$\gamma \propto (V_\theta^+/V_\theta)[a/(\lambda_s^+ d)].$$

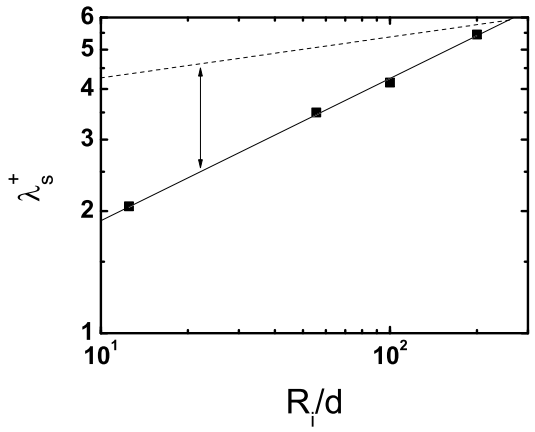

Fig. 17 *Effect of ratio R_i/d on the thickness of the shear band, λ_s^+. The continuous line indicates an approximation of the experimental results ($\lambda_s^+ = 0.84(R_i/d)^{0.35}$). The dashed line represents an overestimation of the glass plate effect on the results ($\lambda_s^+ = 3.41(R_i/d)^{0.10}$).*

Assuming proportionality of γ to the shear band dilation, $\gamma \propto (\Delta\lambda^+/\lambda_s^+)$, the maximum amplitude of ΔV_n might be expressed by: $\Delta V_n^{2-4} \propto (V_\theta^+/V_\theta)(a/d)$.

The results in Fig. 18 are averaged over the three different loads (C_1, C_2 and C_3). The apparent linear relation between ΔV_n^{2-4} and $(V_\theta^+/V_\theta)(a/d)$ is in good agreement with our hypothesis. Macroscopic volumetric variations (ΔV_n^{2-4}) are thus related to the relative sliding velocity at the interface, as expressed by ratio V_θ^+/V_θ, a particle scale effect.

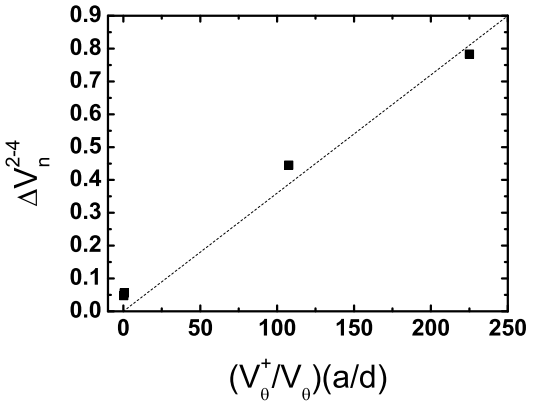

Fig. 18 *Normalized volumetric variation ΔV_n^{2-4} as a function of $(V_\theta^+/V_\theta)(a/d)$. The dotted line is a plot of linear function $\Delta V_n^{2-4} = 0.0036(V_\theta^+/V_\theta)(a/d)$.*

7 Conclusions

The behaviour of the interface between granular materials and a solid body is studied by means of a large $3D$ simple shear annular cell. As boundary conditions, the shear wall velocity V_θ and the radial and vertical confining pressures at the exterior walls are imposed. Roughness and geometrical effects at the resulting shear mobilization are analyzed in macroscopic and mesoscopic scales.

Simple reproducible initial conditions, associated to stable and reproducible interface behaviours are obtained through a cyclic shear procedure with samples composed of model materials (glass beads).

Geometrically, each system is simply described by two nondimensional quantities : R_i/d (where R_i is the internal radius and d the particle diameter), related to the stress distribution and the normalized roughness, R_n.

At the macroscopic scale, the shear stress at the inner cylinder wall, S, and the volumetric variation of the sample, ΔV, are monitored in oscillatory shear experiments, with an amplitude large enough to approach a plateau value in both directions. Since ΔV is concentrated near the interface in strain localized systems, we define a normalized volumetric variation, ΔV_n, to take into account the shearing wall surface and the particle size. Once plotted versus wall displacement, these measurements define cycles, the shape of which stabilizes after a number of oscillations. Steady-state (plateau) values of S and ΔV are growing functions of roughness parameter R_n, approaching finite limits at small R_n (for S and ΔV) and large R_n (for S). In addition, a qualitative cyclic pattern difference is observed, enabling a clearcut distinction between smooth and rough interfaces. At the mesoscopic scale, the radial profiles of the tangential particle velocity $v_\theta(r)$ are obtained by image correlation at the bottom surface of the sample. From these profiles the sliding velocity is measured, which strongly depends on interface roughness. Putting aside this sliding effect, we define a length λ^+ to characterize the shear band thickness.

The analysis of the shear mobilization shows a transient evolution of the shear band thickness. It reaches its maximum at the beginning of the cycle, as does the sample density. The shear stress increase is then followed by material dilation (especially for rough interfaces). Shear band thickness and shear stress both reach a plateau, almost simultaneously, while the relative amount of sliding (V_θ^+/V_θ) keeps a constant value during the entire cycle. Analogously to maximum shear stress, V_θ^+/V_θ increases with roughness level, and approaches finite limits for small and large R_n.

Consistent with the numerical results of [36], our experimental results indicate thicker shear bands for higher values of R_i/d, which is not surprising, as smaller R_i/d entail faster shear stress decay away from the wall. Although the volumetric variation (ΔV_n) keeps increasing for large R_n, this effect is also strongly dependent on geometric effects. Smaller particles induce higher values of R_n, but also higher R_i/d, whence thicker shear bands, the dilation of which resulting in larger values of ΔV_n.

Finally, a more precise description of the volumetric (macroscopic) behaviour is achieved by the association of mesoscopic observations. Assuming all volumetric variation confined within the shear band, we assume its dilation to be proportional to its shear distortion. These assumptions lead to relation $\Delta V_n^{2-4} \propto (V_\theta^+/V_\theta)(a/d)$, between interface dilation (ΔV_n^{2-4}) and relative particle sliding (V_θ^+/V_θ). The correlation of observations at different scales is essential to the characterization and understanding of the behaviour of the interface.

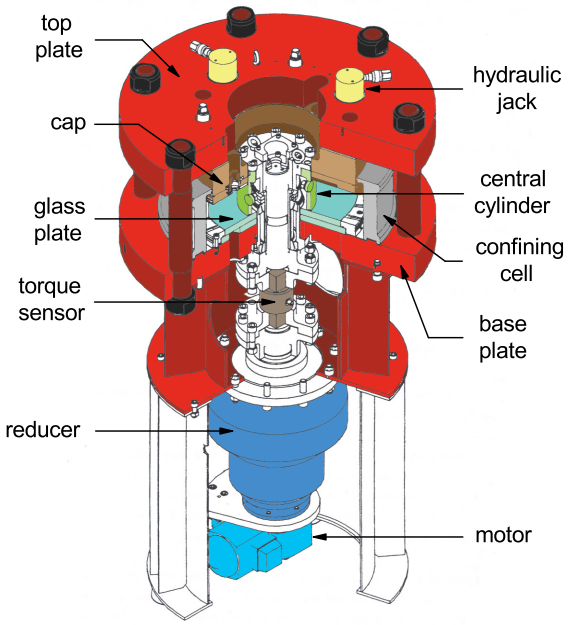

Fig. 19 *Cut-away design view of ACSA.*

A Device description

Fig. 19 shows a cut-away design view of ACSA. The equipment can be divided in two main elements: the structure and the cell. The structure is set on the floor and contains the motor and the reducer which apply the torque on the central cylinder. The gauge torque sensor is placed between the reducer and the central cylinder. The imposed shear velocity V_θ range at the surface of the cylinder varies from 0.1 to 6 mm/min, while a maximal torque of 7000 Nm ($\approx$ 1100 kPa of shear stress at the cylinder wall S) can be achieved. **The torque measure can be affected by friction of different elements of the cell. Calibration tests without samples have shown an increase of 5 ± 1 kPa in shear stress S measure. In our experiences, it represents a maximum error of $\pm 3\%$. The rotation of the cylinder is controlled by an optical encoder with a precision of (VOIR ALAIN).**

In Fig. 20, we show a scheme of the cell. The glass plate is set on the steel base plate of 80 mm thickness by a fixation crown. The base plate has two diametrically opposed windows which allow the visualisation of the sample during the experiments. The steel central cylinder is placed over the glass plate on the central axis of the apparatus.

The sample surrounds the cylinder and is laterally limited by a neoprene® membrane (2 mm of thickness). The glass plate and the cap limit inferiorly and superiorly the sample, respectively, resulting in an annular shape sample.

The cap is composed by a duraluminium and a steel plates with a total mass of 50 kg. Its vertical motion is controlled by three hydraulic jacks set in the top plate (each one with a capacity of 12 t).

The top plate (80 kg of mass) prevents the rotation of the cap, during the shear of the sample, with two vertical guiding axes.

The space between the confining cell and the membrane is filled with water, used to impose the radial confining pressure P_r. The confining cell thickness of 40 mm ensures negligible strain under confining pressures $\leq$ 1000 kPa.

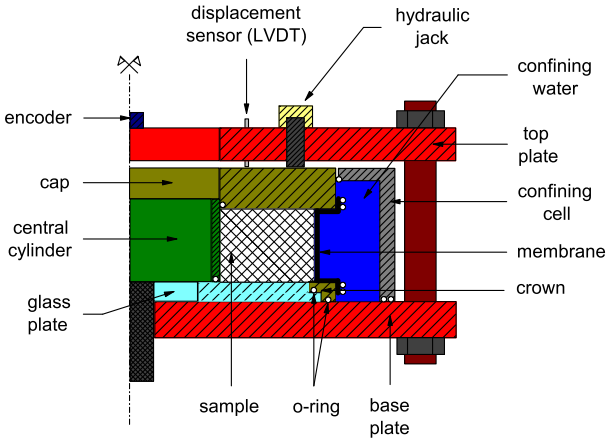

Fig. 20 *Scheme of the shear cell of ACSA.*

The radial and vertical confining pressures (P_r and P_z, respectively) are applied by two pressure-volume controllers GDS® (the first, up to 2 MPa with water, and the second, up to 60 MPa with oil). The first controller provides a direct precision of ± 1 kPa in radial pressure control P_r, associated to a volume precision of ± 1 mm^3. The second controller is associated to three hydraulic jacks in contact with the cap. Calibration tests of the vertical confining pressure P_z [28] have shown a precision of ± 0.6 kPa.

The vertical motion of the cap is measured by 3 displacement transducers (LVDT) of a range and precision of 30 ± 0.075 mm. If we neglect the precise radial component (± 1 mm^3), the volume variation presents at least a precision of $\pm 0.075\%$ of the sample volume.

B Sample preparation

B.1 Cyclic shear procedure and material stabilization

The shear stress in the transient regime strongly depends on the initial state of the sample, especially near the wall. On shearing a dense granular material, significant dilatancy may be observed within the shear zone [38] while outside the shear zone the material may exhibit contraction [39]. In general, transient evolutions depend on the sample preparation method, and initial states get considerably modified as soon as the material deforms. However, beyond a certain level of shear strain in monotonic tests, as the critical state is approached, the material response becomes independent of initial conditions [40–42]. Similarly, experiments of cyclic shear in sand-steel interfaces with a simple shear apparatus [6] showed that after a certain number of cycles, the same shear stress values are observed for samples with different initial density.

Inspired by those observations, we apply repeated shear cycles, so that reproducible and reliable sample initial states are obtained, with no need to control the initial assembling stage in an annular geometry. The inner cylinder is first rotated, with a constant tangential velocity at the wall ($V_\theta = 2$ mm/min), thereby shearing the granular material. When a certain tangential displacement of the cylinder surface is reached, $|D| = a_i$, the imposed motion is stopped and then resumed in the opposite direction (i.e. $V_\theta = -2$ mm/min). A complete cycle corresponds to $4a_i$ of total cylinder tangential displacement (i.e., evaluated, over time T, as $\int_0^T |V_\theta(t)|dt$– see Fig. 5). The displacements are measured by an optical sensor with an accuracy of 2×10^{-2} mm.

We apply a sequence of cycles with increasing amplitude (in cm): $a_1 = 0.5$, $a_2 = 1.5$, $a_3 = 2.5$, $a_4 = 5$, $a_5 = 7.5$ and $a_6 = 10$. 5 cycles are completed for each value a_i before applying larger cycles with value a_{i+1}. All samples behave as shown on Fig. 21: maximum shear stress levels (Fig. 21a) are higher in the first cycles and then tend to stabilize, while the compaction effect (Fig. 21b) gets slower and slower.

Rotation reversals first entail faster volumetric variations. As the sample material compacts and the length of the cycles increases, a dilation phase during the cycle tends to compensate the compaction observed right after the inversion.

This preparation procedure is applied to each new load (first C_2, then C_1 or C_3). In the second and third ones (C_1 and C_3), volumetric stabilization is faster (already achieved in the first cycles) since the initial structure of the sample was already modified under load C_2.

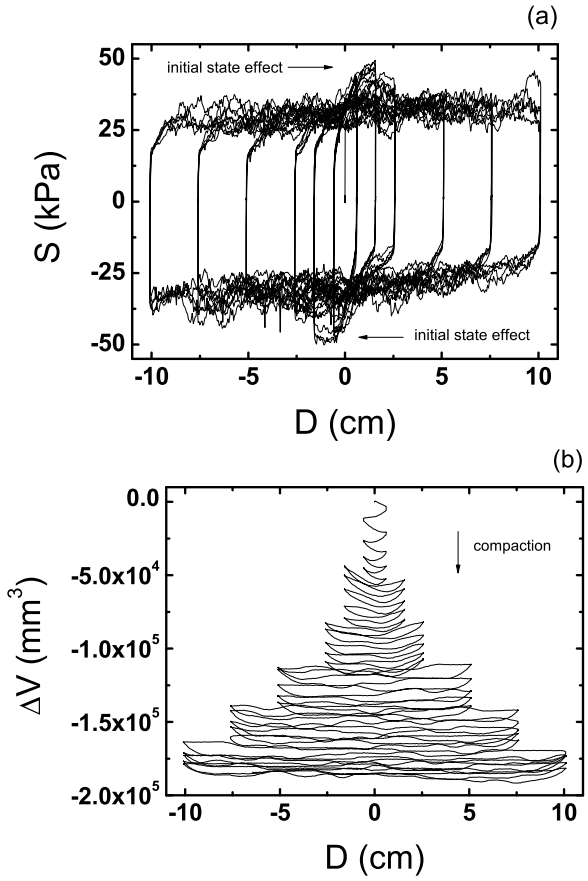

Fig. 21 *Shear stress at the wall S (a) and volumetric variation ΔV (b) versus wall displacement in the first shear cycles. Experiment 2.*

B.2 Influence of cycle size a_i

Fig. 22 shows the typical behaviour of shear stress S and of volumetric variation ΔV for increasing cycle amplitudes a_i. These results are obtained on repeating the sample preparation procedure, i.e., cycle series with 6 growing values of the amplitude, are applied. For each series i ($1 \leq i \leq 6$), the results of Fig. 22 correspond to the fifth (and last) cycle of amplitude a_i, for which the recorded behaviour is deemed stabilized. Originally centered on $D = 0$, the curves are shifted by a_i, so that the fast variations of S and ΔV right after shear reversal points are superimposed. The shear stress first varies rapidly upon shear reversal, then approaches a plateau, and the behaviour is not sensitive to cycle amplitude a_i. As for volumetric variation ΔV (for which the origin on Fig. 22(b) is chosen to coincide with the maximum compaction within each cycle), its fast initial variation after each wall velocity reversal is not sensitive to amplitude a either. Although the slow dilation stage corresponding to the approach of the stress plateau depends on a, the net volumetric change is negligible in all stabilized cycles: on increasing a the slower dilation is compensated by the larger displacement.

All samples in experiments 1 to 7 behave similarly regarding the effect of cycle amplitude. This result allows us to choose one single value of a for further analysis, without loss of generality.

C Influence of the radial and of the vertical confining pressures

In the chosen experimental configuration, we were not allowed to measure the value of the normal stress acting on the interface. Even considering that the confining pressure is well transmitted to the interface through the material (once it is very well sheared and the material is very close to the critical state), the proportion of the effects of each component of the confining stress is not trivial.

For sake of simplicity, we neglect the gravity contribution of $\approx 7\%$ in P_z mean value. Considering the relation between the shear stress at the wall S and the effective pressure P (initially unknown, except for $P_r = P_z$), we defined an *apparent* effective coefficient of friction at the interface $\mu^*_{\text{app}} = S/P$ (apparent because we only suppose the normal stress related to the

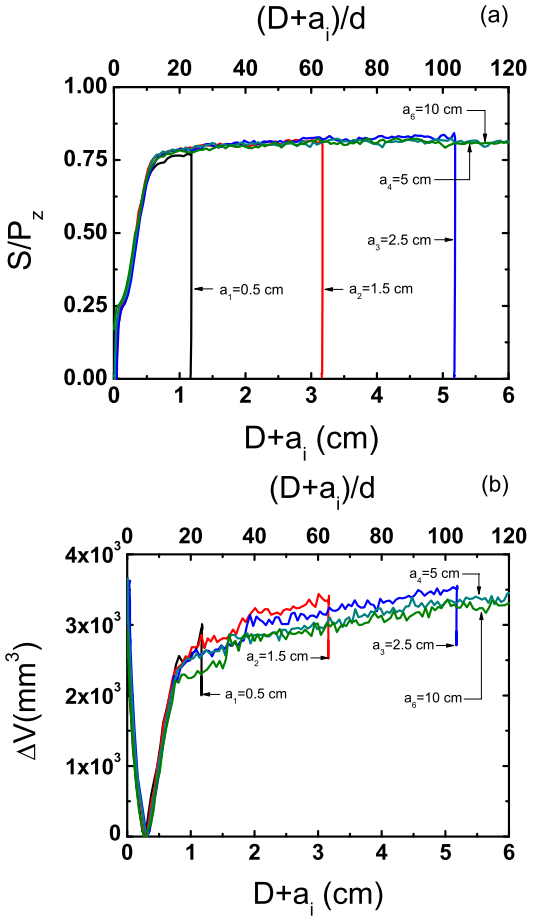

Fig. 22 *Evolution of shear stress at the wall S (a) and volumetric variation ΔV (b) as functions of shifted wall displacement $D + a_i$ for different cycle amplitudes a_i. Experiment 7, load C_2.*

confining pressure). We consider that P is a linear combination of P_r and P_z as follows:

$$P = fP_r + (1 - f)P_z, \tag{9}$$

where f is a distribution coefficient. Therefore, we can write the shear stress at the wall S as

$$S = \mu^*_{\text{app}}(fP_r + (1 - f)P_z). \tag{10}$$

For a single sample, each of the 3 loads (C_1, C_2 and C_3) induces a correspondent value of S. By linear regression, we can determine an approximate value of f and of μ^*_{app} for each sample.

In Fig. 23, we show the values of f obtained from the results of S_4 (shear stress S at the reference point 4) as function of R_n. The observed mean value $\overline{f} = 0.48 \approx 1/2$ suggests that the normal stress at the wall might be simply proportional to $(P_r + P_z)/2$. In other experiments with ACSA developed by [28,43], with the initial state of sand samples controlled by pluviation, a value of f depending on R_n is proposed. With an improved, more complex expression for P, S/P would tend to a single value (μ^*_{app}) even better than shown in Fig. 7b.

With the reduced number of anisotropic loads ($P_r \neq P_z$ - C_1 and C_3) we might expect a certain sensitivity

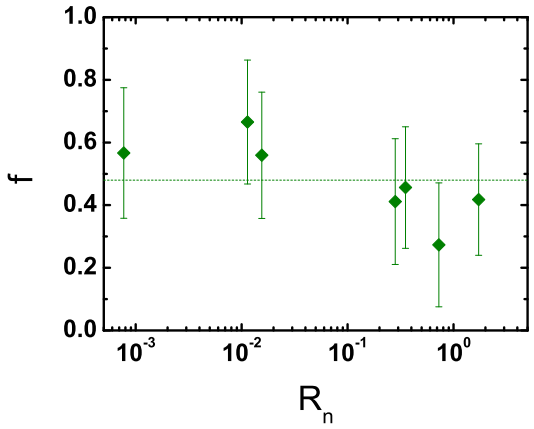

Fig. 23 *Influence of the normalized roughness R_n over the coefficient of pressure distribution f.*

of the values of f with eventual experimental imprecisions (see Appendix A). Considering the precision of P_r (± 1 kPa), P_z (± 7 kPa, considering the gravity), and S (± 1 kPa) maximum absolute errors of almost ± 0.2 are obtained (see Fig. 23).

References

1. J.G. Potyondi. Skin friction between various soils and construction materials. *Géotechnique*, 11(4):339–353, 1961.
2. C.S. Desai, E.C. Drum, and M.M. Zaman. Cyclic testing and modeling of interfaces. *Journal of Geotechnic Engineering*, 111(6):793–815, 1985.
3. M. Uesugi, H. Kishida, and Y. Tsubakihara. Friction between sand and steel under repeated loading. *Soils and foundations*, 29(3):127–137, 1989.
4. M. Uesugi, H. Kishida, and Y. Uchikawa. Friction between dry sand and concrete under monotonic and repeated loading. *Soils and Foundations*, 30(1):115–128, 1990.
5. J.T. DeJong, M.F. Randolph, and D.J. White. Interface load transfer degradation during cyclic loading: a microscale investigation. *Soils and Foundations*, 43(4):81–93, 2003.
6. T.A. Oumarou and E. Evgin. Cyclic behaviour of a sand-steel plate interface. *Can. Geotech. J.*, 42:1695–1704, 2005.
7. M. Toiya, J. Stambaugh, and W. Losert. Transient and oscillatory granular shear flow. *Phys. Rev. Lett.*, 93(8):088001, Aug 2004.
8. M. Uesugi, H. Kishida, and Y. Tsubakihara. Behavior of sand particules in sand-steel friction. *Soils and foundations*, 28(1):107–118, 1988.
9. L. Chevalier, S. Calloch, F. Hild, and Y. Marco. Digital image correlation used to analyze the multiaxial behaviour of rubber-like materials. *Eur. J. Mech. A*, 20:168–187, 2001.
10. F. Hild, J.-N. Périé, and M. Coret. Mésures de champs de déplacement 2d par corrélation d'images numériques : Correli^{2D}. Internal Report 230, LMT-Cachan, 1999.
11. F. Hild, B. Raka, M. Baudequin, S. Roux, and F. Cantelaube. Multiscale displacement field measurements of compressed mineral-wool samples by digital image correlation. *Applied Optics*, 41(32):6815–6828, 2002.
12. G. Chambon, J. Schmittbuhl, A. Corfdir, J.-P. Vilotte, and S. Roux. Shear with comminution of a granular material: Microscopic deformations outside the shear band. *Phys. Rev. E*, 68:011304, 2003.

13. D. Howell, R.P. Behringer, and C.T. Veje. Stress fluctuations in a 2d granular Couette experiment : a continuum transition. *Phys. Rev. Lett.*, 82:5241–5244, 1999.
14. W. Losert and G. Kwon. Transition and steady-state dynamics of granular shear flows. *Advances in complex systems*, 4:369–377, 2001.
15. D.M. Mueth, G.F. Debregeas, G.S. Karczmar, P.J. Eng, S.R. Nagel, and H.M. Jaeger. Signature of granular microstructure in dense shear flows. *Nature*, 406:385–389, 2000.
16. C.T. Veje, D.W. Howell, and R.P. Behringer. Kinematics of two - dimensional granular Couette experiment at the transition to shearing. *Phys. Rev. E*, 59:739–745, 1999.
17. P. Lerat. *Etude de l'interface sol - structure dans les milieux granulaires à l'aide d'un nouvel appareil de cisaillement annulaire.* PhD thesis, École nationale des ponts et chaussées, Paris, 1996.
18. P. Unterreiner. *Contribution à l'étude et à la modélisation des sols cloués : application en calcul en déformation des ouvrages de soutènement.* PhD thesis, École nationale des ponts et chaussées, Paris, 1994.
19. I. Vardoulakis, K. R. Shah, and P. Papanastasiou. Modeling of tool-rock interfaces using gradient dependent flow-theory of plasticity.
20. P. Unterreiner and I. Vardoulakis. Interfacial localization in granular media. In Siriwardane and Zaman, editors, *Computer Methods in Geomechanics*, pages 1711–1715, Balkema, 1994.
21. A. Zervos, I. Vardoulakis, M. Jean, and P. Lerat. Numerical investigation of granular kinematics. *Mechanics of Cohesive-Frictional Materials*, 4:305–324, 2000.
22. A. Corfdir, P. Lerat, and I. Vardoulakis. A cylinder shear apparatus. *Geotechnical Testing Journal*, 27(5):447–455, 2004.
23. M. Uesugi and H. Kishida. Influential factors of friction between steel and dry sands. *Soils and Foundations*, 26(2):33–46, 1986.
24. L. Bocquet, W. Losert, D. Schalk, T. C. Lubensky, and J. P. Gollub. Granular shear flow dynamics and forces : Experiment and continuous theory. *Phys. Rev. E*, 65:011307, 2002.
25. D.M. Mueth. Mesurement of particule dynamics in slow, dense granular couette flow. *Phys. Rev. E*, 67:011304, 2003.
26. G. Chambon. *Caractérisation expérimentale du frottement effectif des zones de faille.* PhD thesis, ENPC, 2003.
27. P. Moucheront, F. Bertrand, G. Koval, L. Tocquer, S. Rodts, J.-N. Roux, A. Corfdir, and F. Chevoir. Mri investigation of granular interface rheology using a new cylinder shear apparatus. *Magnetic Resonance Imaging*, doi: 10.1016/j.mri.2010.01.007.
28. A.I. Dumitrescu. *Étude expérimentale du comportement d'interface sol grenu / stucture.* PhD thesis, École nationale des ponts et chaussées, Paris, 2005.
29. Y.B. Acar, T. Durgunoglu, and M. Tumay. Interface properties of sand. *Journal of the Soil Mechanics and Foundation Division*, 108(GT4):648–655, 1982.
30. W.F. Brumund and G.A. Leonards. Experimental study of static and dynamic friction between sand and typical construction materials. *Journal of Testing and Evaluation*, 1(2):163–165, 1973.
31. Y. Yoshimi and T. Kishida. A ring torsion apparatus for evaluating friction between soil and metal interfaces. *Geotechnical Testing Journal*, 4(4):145–152, 1981.
32. S.G. Paikowsky, C.M. Player, and P.J. Connors. A dual interface apparatus for testing unrestricted friction of soil along solid surfaces. *Geotechnical Testing Journal*, 18(2):168–193, 1995.
33. J. Tejchman and W. Wei. Experimental and numerical study on steel - sand interfaces. *International journal for numerical and analytical methods in geomechanics*, 19:513–536, 1995.
34. M. Lätzel. *From microscopic simulations towards a macroscopic description of granular media.* PhD thesis, University of Stuttgart, Stuttgart, 2003.
35. F. Chevoir, M. Prochnow, P. Moucheront, F. da Cruz, F. Bertrand, J.P. Guilbaud, P. Coussot, and Roux J.N. Dense granular flows in a vertical chute. In Kishino, editor, *Powders and grains 2001*, pages 399–402, Lisse, 2001. Swets and Zeitlinger.
36. G. Koval, J.-N. Roux, A. Corfdir, and F. Chevoir. Annular shear of cohesionless granular materials: From the inertial to quasistatic regime. *Phys. Rev. E*, 79(2):021306, 2009.
37. G. Koval. *Comportement d'interface des matériaux granulaires.* PhD thesis, Ecole Nationale des Ponts et Chaussées, 2008.
38. J. Desrues, R. Chambon, M. Mokni, and F. Mazerolle. Void ratio evolution inside shear bands in triaxial sand specimens studied by computed tomography. *Géotechnique*, 46(3):529–546, 1996.
39. J. Tejchman and E. Bauer. Fe-modeling of shear resistance degradation in granular materials during cyclic shearing under cns condition. *Computers and Geotechnics*, 2008.
40. A. N. Schofield and C. P. Wroth. *Critical state in soil mechanics.* Mc Graw-Hill, New York, 1968.
41. D. M. Wood. *Soil Behaviour and Critical State Soil Mechanics.* Cambridge University Press, 1990.
42. F. Radjai and S. Roux. Turbulentlike fluctuations in quasistatic flow of granular media. *Phys. Rev. Lett.*, 89(6):064302, 2002.
43. A. Dumitrescu, A. Corfdir, and R. Frank. Influence of the anisotropy of confining stress on the sand/steel interface behaviour in a cylinder shear apparatus. *Soils and foundations*, 49(2):167–174, 2009.